

# Quasi-Static Three-Point Bending of Carbon Fiber Sandwich Beams With Square Honeycomb Cores

B. P. Russell<sup>1</sup>

T. Liu

N. A. Fleck

V. S. Deshpande

Department of Engineering,  
University of Cambridge,  
Trumpington Street,  
Cambridge CB2 1PZ, UK

Sandwich beams comprising identical face sheets and a square honeycomb core were manufactured from carbon fiber composite sheets. Analytical expressions were derived for four competing collapse mechanisms of simply supported and clamped sandwich beams in three-point bending: core shear, face microbuckling, face wrinkling, and indentation. Selected geometries of sandwich beams were tested to illustrate these collapse modes, with good agreement between analytic predictions and measurements of the failure load. Finite element (FE) simulations of the three-point bending responses of these beams were also conducted by constructing a FE model by laying up unidirectional plies in appropriate orientations. The initiation and growth of damage in the laminates were included in the FE calculations. With this embellishment, the FE model was able to predict the measured load versus displacement response and the failure sequence in each of the composite beams. [DOI: 10.1115/1.4003221]

**Keywords:** sandwich beam, honeycomb core, composite, damage mechanics

## 1 Introduction

Sandwich structures comprising face sheets made from a strong and stiff material separated by a low density core are extensively used in lightweight structures because of their high specific stiffness and strength. The cores of such structures require high shear and compressive strength to resist failure of such sandwich beams by core shear or core indentation, respectively.

Sandwich cores have evolved from stochastic metallic and polymeric foams to periodic lattice materials with high nodal connectivities of their trusslike microstructures. The motivation for this evolution is that the strength of foams is governed by the bending of the cell walls and scales as  $\bar{\rho}^{3/2}$ , where  $\bar{\rho}$  is the relative density of the foam (Ashby et al. [1], Deshpande et al. [2], Gibson and Ashby [3]), while lattice materials deform by cell wall stretching and thus have a strength that scales linearly with  $\bar{\rho}$ . Thus, for a relative density of  $\bar{\rho}=0.1$ , the lattice material is about three times stronger than the corresponding foam. Typically, lattice material topologies include the pyramidal truss [4], square honeycombs, and prismatic corrugated cores (Côté et al. [5] and Côté et al. [6]). To date, these cores have been predominantly metallic due to the wide range of metallic fabrication techniques available; see, for example, Wadley et al. [4]. Further enhancements in specific strength and stiffness are realized by constructing these sandwich cores from composites of high specific properties. The composite lattice core systems studied to date include carbon fiber pyramidal trusses (Finnegan et al. [7]), carbon fiber honeycombs (Russell et al. [8]), and carbon fiber corrugated cores (Kazemahvazi and Zenkert [9] and Kazemahvazi et al. [10]). These composite sandwich cores have higher strength, stiffness, and energy absorption on a unit mass basis compared with their metallic counterparts (Finnegan et al. [7] and Russell et al. [8]).

Sandwich beams are used increasingly in applications requiring high bending stiffness and strength combined with low weight. The concept of the structural sandwich beam—the separation of stiff faces by a lightweight core—dates back to the 1820s (Zenkert

[11]), but the systematic use of sandwich beams and sandwich panels as structural elements only gained acceptance in the middle of the 20th century for aircraft structures. Plantema [12], Allen [13], and Zenkert [11] summarized the literature on sandwich beams, including a systematic design strategy for stiffness and strength. It has long been recognized that sandwich beams fail by a number of competing mechanisms; Gibson and Ashby [3] generated collapse mechanism maps for beams in bending to show the dependence of the failure mode upon the geometry of beams and the relative strength of the faces and cores. Although their approach was first demonstrated for aluminum alloy face sheets and polymeric foam cores, it has since been extended to other combinations such as metallic face sheets and metallic foam cores; see, for example, Chen et al. [14] and McCormack et al. [15]. Failure maps for elastic-brittle sandwich beams have been developed by Petras and Sutcliffe [16] and by Shenhar et al. [17]. These are based on the higher-order sandwich theory of Frostig and co-workers; see, for example, Frostig et al. [18] and Frostig and Baruch [19]. This approach, although mathematically sound, has been largely superseded by finite element (FE) codes, which allow for geometric and material nonlinearity. Steeves and Fleck [20] and Tagarielli et al. [21] presented a combined experimental and numerical finite element investigation of the three-point bending response of simply supported and clamped sandwich beams made from glass-epoxy face sheets and a polymer foam core. A detailed review of recent findings of the failure modes of composite beams with foam cores has been presented by Daniel and Gdoutos [22], and readers are referred to an anthology on composite materials and sandwich structures edited by Daniel et al. [23] for a more complete review of the literature on composite sandwich beams with foam cores.

**1.1 Scope and Novelty of the Study.** To date, there has been little or no measurement or modeling of composite sandwich beams with lattice cores—as discussed above, enhancements in performance are expected by replacing the foam core with a lattice material. This paper thus has two objectives. First, we investigate the bending response of a composite sandwich beam with a novel lattice core over a wide range of beam geometries. In particular, we manufacture and test sandwich beams with face sheets and square honeycomb cores each made from a carbon fiber composite; the beams are loaded in three-point bending, with both

<sup>1</sup>Corresponding author.

Contributed by the Applied Mechanics of ASME for publication in the JOURNAL OF APPLIED MECHANICS. Manuscript received November 2, 2010; final manuscript received December 7, 2010; accepted manuscript posted December 9, 2010; published online February 15, 2011. Assoc. Editor: Robert M. McMeeking.

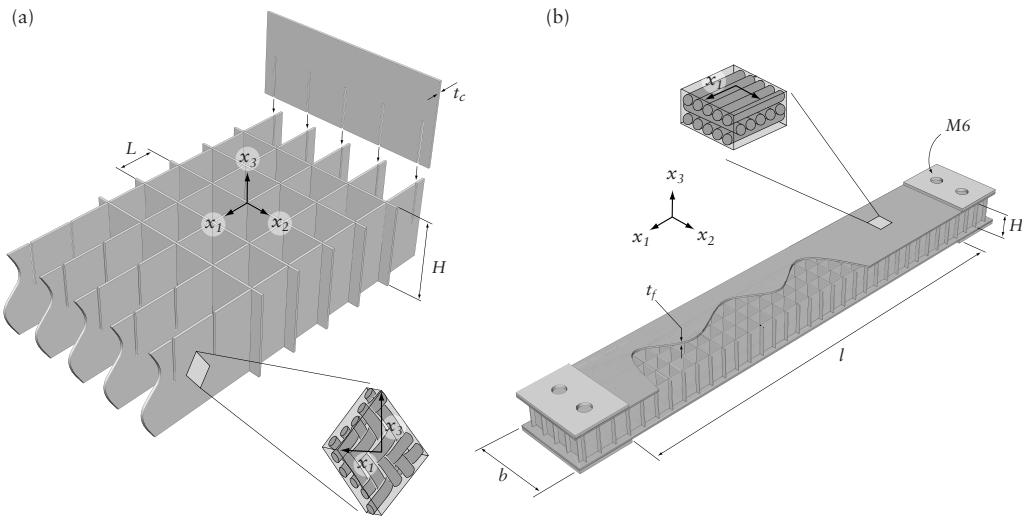


**Fig. 1 Sketches of the slotting technique used to assemble (a) the square honeycomb sandwich cores and (b) the assembled sandwich beams. The coordinate system associated with the core and beam and the notation used to indicate the dimensions of the honeycomb core and sandwich beam are included.**

simply supported and clamped boundary conditions. The second objective of this study is to investigate the fidelity of the appropriately calibrated constitutive models of Matzenmiller et al. [24] and Hashin [25] in predicting damage progression in the composite sandwich beams. This is achieved by constructing detailed 3D FE models that include all the geometric details of the beams and cores.

The outline of this paper is as follows. First, the composition and geometry of the composite sandwich beams are described, and the manufacturing route is detailed. Second, analytical expressions for the various collapse mechanisms of the sandwich beams are used to guide the design of sandwich beam geometries. The three-point bend tests on the clamped and simply supported beams are discussed. Finally, finite element predictions are compared with the measured response and with the observed collapse mechanisms.

## 2 Materials and Manufacture

A range of geometries of carbon fiber composite sandwich beams comprising a square honeycomb core and two identical face sheets were manufactured and tested in three-point bending in both simply supported and end-clamped configurations.

**2.1 Materials.** The square honeycomb core was manufactured by slotting together woven carbon fiber composite sheets of thickness  $t_c=0.35$  mm and density  $\rho=1370 \text{ kg m}^{-3}$ . The composite sheets comprised Toray T300-6k fibers (of diameters 6–7.5  $\mu\text{m}$ ) arranged in a  $2\times 2$  twill weave architecture with 0.37 tows/mm. The fibers were embedded within a Fiberite 934 high-heat resistant epoxy. The two face sheets of the sandwich beams comprised 0–90 deg laminates with IM7-12k carbon fibers embedded within a HexPly® 8552 resin system. Each ply of the laminate was approximately 0.25 mm thick with a density  $\rho=1570 \text{ kg m}^{-3}$ ; 3–16 plies were stacked in order to obtain face sheets of thickness in the range  $t_f=0.75$ –4 mm.

**2.2 Manufacture of the Core and Sandwich Beams.** The square honeycomb cores were manufactured using the method developed by Russell et al. [8], and so a brief summary suffices here. Composite sheets were cut into strips of width in the range 10.5–60 mm. This width direction of the strip is aligned with the height direction of the core, as shown in Fig. 1(a); also, the fiber tows were oriented at  $\pm 45$  deg within each strip. The strips were either of length 250 mm (corresponding to the lengths of the

beams in Fig. 1(b)) or of length 35 mm (corresponding to the width  $b$  of the beams). Slots of height  $H/2$ , width  $\Delta t_c=45 \mu\text{m}$ , and spacing  $L=7.1$  mm were machined into the strips using a two-axis milling machine. The slotted strips were then assembled to form square honeycombs of height  $H$ , length of 250 mm, width of 35 mm, and relative density  $\bar{\rho}=0.1$  (see Fig. 1(a)). After assembly, a low viscosity epoxy (Opti-tec 5001<sup>2</sup>) adhesive was applied to the joints of the stand-alone core: The epoxy was cured in air at 65°C for 1 h.

The faces of the sandwich beams comprised a symmetric laminate of 0 deg/90 deg layers, with the 0 deg orientation along the  $x_1$  axis of the beam (recall Fig. 1(a)). The thickness  $t_f$  of the faces was varied by altering the number of plies in the stack. For example, faces of thickness  $t_f=0.75$  mm were of lay-up (0 deg/90 deg/0 deg), whereas the  $t_f=4$  mm faces made from 16 plies were of lay-up [(0 deg/90 deg)<sub>8</sub>]. The beam face sheets of 250 mm length and 35 mm width were cut from the cured laminated sheets using a diamond saw. In the final assembly operation, the faces were bonded to the square honeycomb core via a nylon backed film epoxy (Redux 319<sup>3</sup> with an areal density of 400 gm<sup>-2</sup>): This epoxy film was placed on one side of each of the face sheets, and the sandwich assembly, comprising face sheets and core, was oven cured at 175°C for 1 h. A sketch of the final assembled sandwich beam and its leading dimensions is given in Fig. 1(b).

Some additional steps were involved in the manufacture of the end-clamped beams. The clamping fixture is sketched in Fig. 2(a) and was used to clamp the beams over an end portion of 25 mm, thereby minimizing rotations and deflections of the ends of the beam. The honeycomb cores of the sandwich beams were filled with an epoxy (Biresin® G30<sup>4</sup>) over the 25 mm clamped portion (three rows of cells), as sketched in Fig. 2(b), thereby enabling high clamping pressures to be applied via M6 bolts.

**2.3 Mechanical Properties of the Composite Face Sheets and Core.** The quasi-static uniaxial compressive and tensile responses of the composite materials were measured at an applied nominal strain rate of  $10^{-3} \text{ s}^{-1}$  using the procedure detailed in Russell et al. [8]. In brief, dog-bone-shaped specimens were cut

<sup>2</sup>Intertronics, 17 Station Field Industrial Estate, Banbury Road, Kidlington, Oxfordshire OX5 1JD, UK.

<sup>3</sup>Excel Composites, Duxford, UK.

<sup>4</sup>Sika, Watchmead, Welwyn Garden City, Hertfordshire AL7 1BQ, UK.

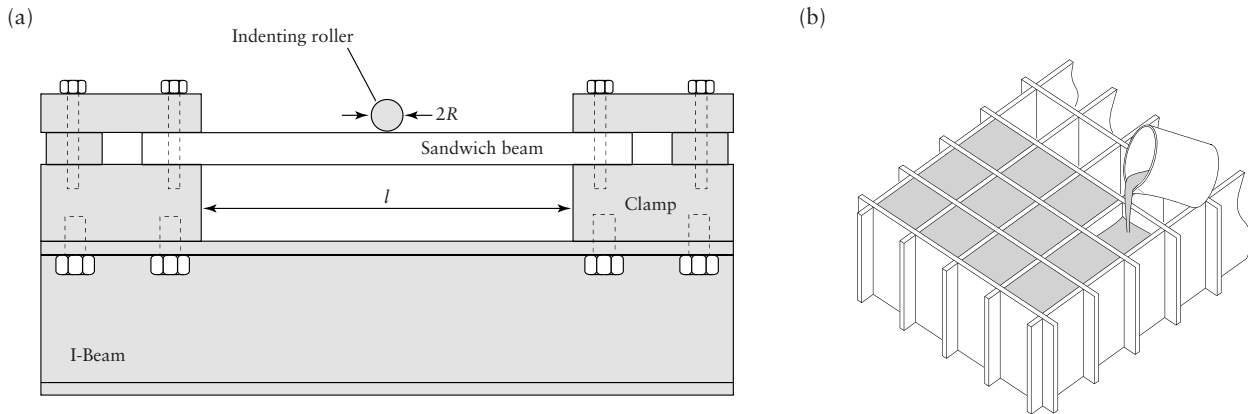


**Fig. 2 Sketches of (a) the clamping fixture for the sandwich beams and (b) the sandwich beams with end portions filled with epoxy so as to allow high clamping pressures to be applied**

from the composite face sheets and core strips (prior to slotting). The tensile responses were measured by friction gripping of these specimens and by conducting tensile tests in a screw-driven test machine. The applied load was measured via the load cell of the test machine and was used to define the applied stress, while a 0–90 deg strain gauge rosette was used to measure the axial and transverse strain components. In order to perform compression tests that do not lead to premature failure by Euler buckling of the specimens, a sandwich column with faces constructed from the face sheets of the composite material and an aluminum hexagonal honeycomb core. The compression tests were also performed in the screw-driven test machine, with the loads and strain measured in a similar manner to that described for the tensile tests.

The measured tensile and compressive responses of the face sheet material (comprising two orthogonal unidirectional plies) and the woven composite core material are plotted in Figs. 3(a) and 3(b), respectively. Both the laminate and woven materials were tested in the 0–90 deg and ±45 deg orientations. In the 0–90 deg orientation, both the laminate and woven materials display an elastic-brittle response in compression and in tension. The modulus of the 0–90 deg oriented laminate is  $E_l^0=85$  GPa, while its compressive and tensile strengths are  $\sigma_l^{0c}=630$  MPa and  $\sigma_l^{0t}=980$  MPa, respectively. The corresponding values for the woven

material are  $E_w^0=63$  GPa,  $\sigma_w^{0c}=330$  MPa, and  $\sigma_w^{0t}=540$  MPa. In contrast, the response of both the laminate and woven materials in the ±45 deg orientation is dominated by the shear of the matrix, and hence the composites display a ductile response in both tension and compression. The (unloading) modulus of the laminate is  $E_l^{45}=16$  GPa, while the tensile and compressive strengths are  $\sigma_l^{45t}=115$  MPa and  $\sigma_l^{45c}=215$  MPa, respectively. The corresponding properties of the woven material are  $E_w^{45}=16$  GPa,  $\sigma_w^{45t}=175$  MPa, and  $\sigma_w^{45c}=190$  MPa. These values are listed in Table 1 and are used in the analytical and finite element calculations.

The compressive ( $\sigma_{33}$  versus  $\varepsilon_{33}$ ) and shear ( $\tau_{13}$  versus  $\gamma_{13}$ ) responses of the  $\bar{p}=0.1$  composite square honeycomb have been reported previously by Russell et al. [8]. These measurements are replotted in Fig. 4. The compressive and shear moduli of the core are  $E_c=3.1$  GPa and  $G_c=0.6$  GPa, respectively, while the corresponding strengths are  $\sigma_c=12.2$  MPa and  $\tau_c=6.1$  MPa. The properties of the composite face sheets and the effective properties of the honeycomb core (all listed in Table 1) are used in analytical predictions of the stiffness and collapse strength of the sandwich beams.

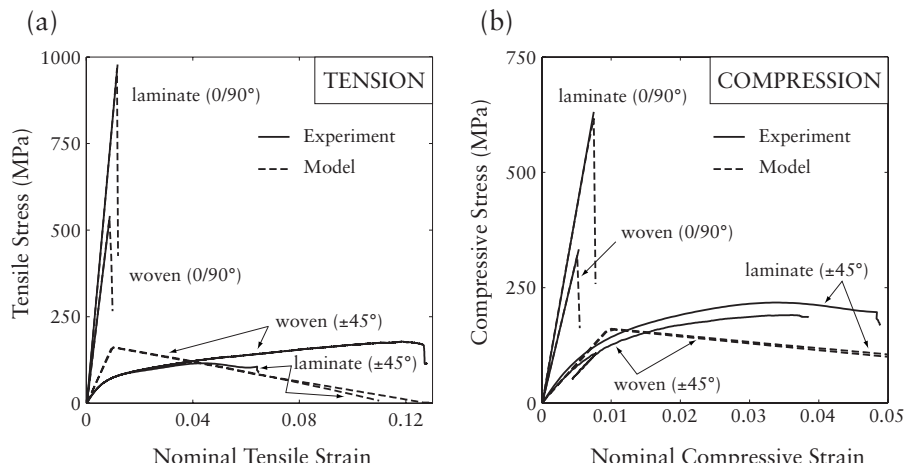


**Fig. 3 The measured tensile and compressive quasi-static stress versus strain responses of the (a) laminate composite (comprising two orthogonal unidirectional plies) and (b) the woven composite materials. The responses are shown for both the 0–90 deg and ±45 deg orientations. The corresponding predictions of the calibrated constitutive model are also included.**

**Table 1** The measured material properties of the laminate (comprising two orthogonal unidirectional plies) and woven composite materials. The measured effective properties of the square honeycomb sandwich core are also listed.

Material	Property	Value (MPa)
Woven	$E_w^0$	63,000
	$E_w^{45}$	16,000
	$\sigma_{w,t}^0$	540
	$\sigma_{w,c}^0$	330
	$\sigma_{w,45t}^0$	175
	$\sigma_{w,45c}^0$	190
Laminate	$E_l^0$	85,000
	$E_l^{45}$	16,000
	$\sigma_{l,t}^0$	980
	$\sigma_{l,c}^0$	630
	$\sigma_{l,45t}^0$	115
	$\sigma_{l,45c}^0$	215
Square honeycomb core	$E_c$	3100
	$G_c$	590
	$\sigma_c$	12.2
	$\tau_c$	6.1

### 3 Analytical Predictions of the Response of the Beams in Three-Point Bending

We begin by summarizing analytical formulas for the stiffness and collapse strength of clamped and simply supported sandwich beams in three-point bending, assuming that the core and face sheets are homogeneous. The main aim of this simplified approach is to develop a basic understanding of the collapse mechanisms to aid the design of the sandwich beam geometries for the experimental program, rather than develop a highly accurate analytical model.

Consider a sandwich beam of span  $\ell$  and width  $b$  comprising identical face sheets of thickness  $t_f$  and a core of thickness  $H$  (Fig. 5). In the simply supported configuration, the beam is supported on circular cylindrical rollers of radius  $R$  spaced a distance  $\ell$  apart with the load  $F$  applied via a central roller also of radius  $R$ . The simply supported beams have an overhang  $s$  beyond the outer supports (Fig. 5(a)). The clamped beams have a span  $\ell$  between the clamped ends and are also centrally loaded by a load  $F$  via the circular cylindrical roller of radius  $R$  (Fig. 5(b)).

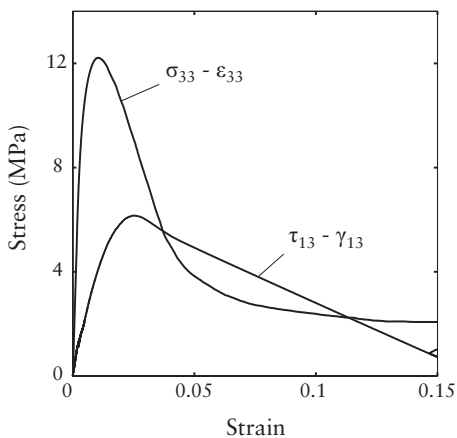


**Fig. 4** The measured compressive ( $\sigma_{33} - \varepsilon_{33}$ ) and shear ( $\tau_{13} - \gamma_{13}$ ) responses of the  $\bar{\rho}=0.1$  composite square honeycomb core. From Russell et al. [8].

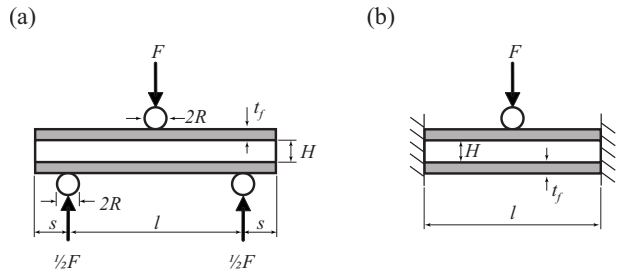


**Fig. 5** Sketches of the loading configuration of the sandwich beams in the (a) simply supported and (b) clamped configurations

**3.1 Formulas for the Stiffness.** The relative deflection  $\delta$  of the central roller with respect to the supports is the sum of the bending and shear deflections (Allen [13]) and is given by

$$\delta = \frac{F\ell^3}{48(EI)_{eq}} + \frac{F\ell}{4(AG)_{eq}} \quad (3.1)$$

and

$$\delta = \frac{F\ell^3}{192(EI)_{eq}} + \frac{F\ell}{4(AG)_{eq}} \quad (3.2)$$

for the simply supported and clamped beams, respectively. The flexural rigidity, including contributions from the core, faces, and sandwich construction, is

$$(EI)_{eq} = \frac{nE_w^{45}t_cH^3}{12} + \frac{E_fbt_f^3}{6} + \frac{E_fbt_f(H+t_f)^2}{2} \quad (3.3)$$

where  $n$  is the number of walls of the honeycomb core along the width  $b$  of the beam (Fig. 1(b)), while  $E_f$  is the effective Young's modulus of the face-sheet material along the  $x_1$  axis according to the standard laminate plate theory. The shear rigidity is given as

$$(AG)_{eq} = G_c b H \quad (3.4)$$

where  $G_c$  is the effective shear modulus of the core as measured from the shear stress  $\tau_{13}$  versus shear strain  $\gamma_{13}$  response.

**3.2 Collapse Mechanisms.** We now proceed to give simple analytical expressions for the initial collapse load of the beams for four possible collapse mechanisms: (a) face microbuckling, (b) core shear, (c) core indentation, and (d) face wrinkling (see Fig. 6). The operative collapse mechanism is the one that has the lowest load for the given beam geometry.

**3.2.1 Core Shear.** The failure load for core shear is obtained by equating the maximum stress in the core, as given by an elastic

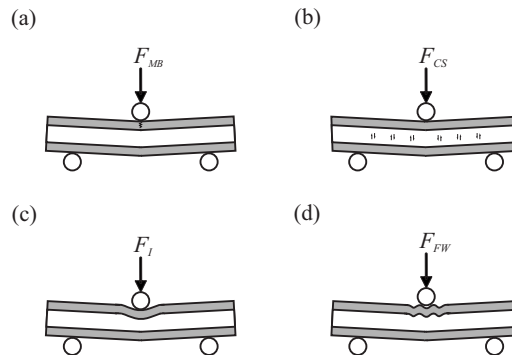


**Fig. 6** Sketches illustrating the four principal collapse modes of the clamped and simply supported composite sandwich beams

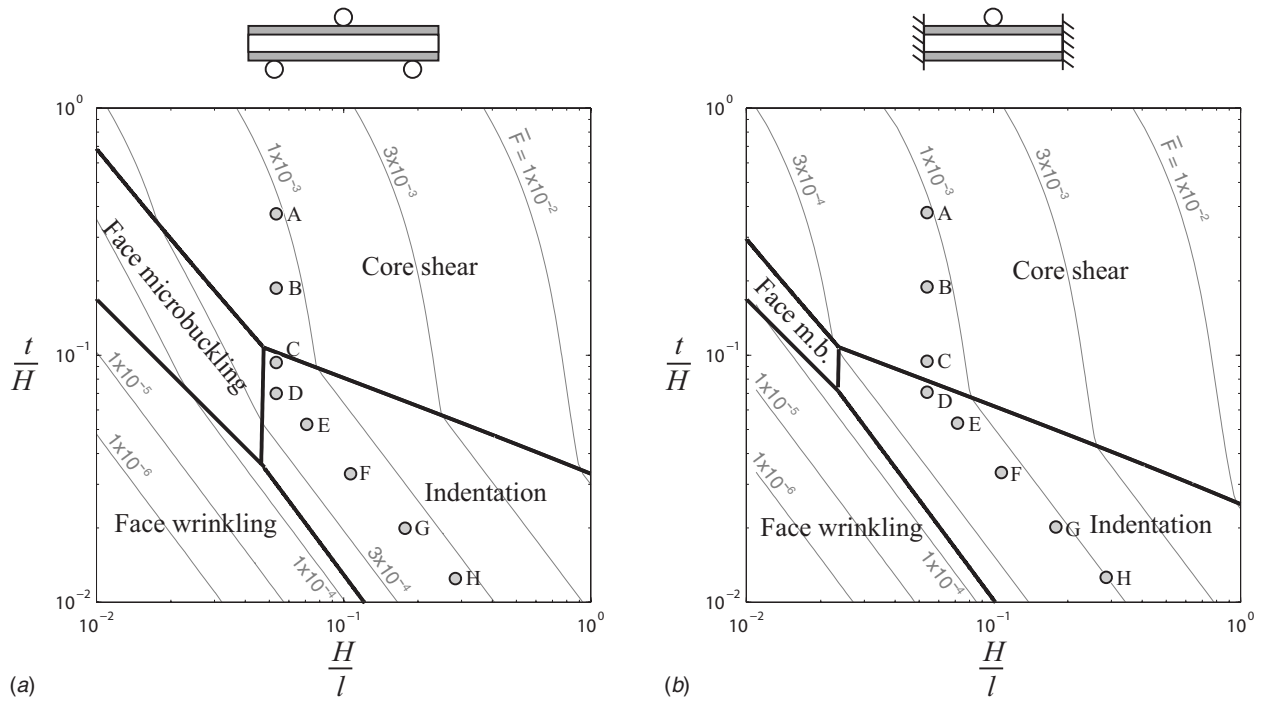


**Fig. 7 Collapse mechanism maps for the (a) simply supported and (b) clamped sandwich beams with a square honeycomb core of relative density  $\bar{\rho}=0.1$ . The beams have  $n=5$  walls across the width  $b$  of the beams. The geometries tested in this study are marked on the map along with contours of the nondimensional collapse load  $\bar{F}$ .**

sandwich beam analysis (Allen [13]), to the core shear strength  $\tau_c$ . For both simply supported and clamped beams, this gives

$$F_{CS} = \frac{16\tau_c(EI)_{eq}}{4E_f t_f (H + t_f) + nE_w^{45} \left(\frac{t_c}{b}\right) H^2} \quad (3.5)$$

**3.2.2 Face Microbuckling.** Under macroscopic bending of the sandwich beam, the upper face sheet is in compression while the lower face sheet is in tension. The compressive face sheet may fail by microbuckling of the composite. Equate the maximum stress in the face sheet as given by an elastic analysis (Allen [13]) to the microbuckling strength  $\sigma_{MB}$  of the face-sheet material. To make accuracy adequate,  $\sigma_{MB}$  scales with  $\sigma_l^{0c}$  according to the laminate plate analysis (i.e., a Voigt upper bound). The microbuckling failure load then follows as

$$F_{MB} = 4\sigma_{MB} \frac{(EI)_{eq}}{E_f \ell (H/2 + t_f)} \quad (3.6)$$

for simply supported beams and

$$F_{MB} = 8\sigma_{MB} \frac{(EI)_{eq}}{E_f \ell (H/2 + t_f)} \quad (3.7)$$

for clamped beams.

**3.2.3 Face Wrinkling.** The face sheet under compression can also fail by buckling or wrinkling with a wavelength equal to the cell size of the square honeycomb core. The elastic buckling or wrinkling load of the laminate face sheet simply supported by the honeycomb core of cell size  $L$  is given by (Roark and Young [26])

$$\sigma_{FW} \approx 3.3E_f \left(\frac{t_f}{L}\right)^2 \quad (3.8)$$

The face wrinkling load  $F_{FW}$  for simply supported and clamped beams follows immediately upon replacing  $\sigma_{MB}$  by  $\sigma_{FW}$  in Eqs. (3.6) and (3.7), respectively.

**3.2.4 Core Indentation.** The indentation failure load for sandwich beams with elastic faces upon a core of compressive strength  $\sigma_c$  was derived by Steeves and Fleck [20]. For simply supported and clamped beams, respectively, the collapse load reads

$$F_I = b t_f \left( \frac{\pi^2 (H + t_f) E_f \sigma_c^2}{3\ell} \right)^{1/3} \quad (3.9)$$

and

$$F_I = b t_f \left( \frac{2\pi^2 (H + t_f) E_f \sigma_c^2}{3\ell} \right)^{1/3} \quad (3.10)$$

**3.3 Collapse Mechanism Maps.** It is assumed that the operative collapse mechanism for a sandwich beam is the one associated with the lowest collapse load. This can be shown graphically by plotting a nondimensional measure of the collapse load,

$$\bar{F} = \frac{F}{b\ell\sigma_{MB}} \quad (3.11)$$

on a diagram with nondimensional axes  $H/\ell$  and  $t/H$  for a given combination of face-sheet and core materials.

Collapse mechanism maps are shown in Figs. 7(a) and 7(b) for the simply supported and clamped composite beams, respectively. In plotting these maps, we have assumed that the beam material combination is that described in Sec. 2, i.e., laminated composite face sheets and a square honeycomb core of relative density  $\bar{\rho}=0.1$ , made from a woven composite. The beams have a width  $b=35$  mm, and thus the core has  $n=5$  walls across the width. The measured material properties of the face sheets  $E_l^0$  and  $\sigma_l^{0c}$  and core properties  $E_w^{45}$ ,  $\sigma_c$ , and  $\tau_c$  (Sec. 2.3) are used in Eqs. (3.5)–(3.10) for the construction of the maps. The regimes of dominance of each failure mode are marked on the maps. Core shear and core indentation are the dominant collapse modes for

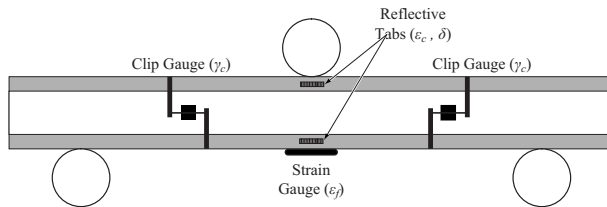


**Fig. 8 Sketch illustrating the instrumentation employed to measure the core compression strain  $\varepsilon_c$ , core shear strain  $\gamma_c$ , face-sheet strain  $\varepsilon_f$ , and the roller displacement  $\delta$**

both simply supported and clamped beams; in contrast, face microbuckling dominates over a very limited range of beam geometries.

#### 4 Measurement of Bend Response

The bend tests on the clamped and simply supported beams were conducted in a screw-driven test machine. The beams were loaded by a cylindrical roller of radius  $R=19$  mm displaced at a fixed rate of  $0.2 \text{ mm min}^{-1}$ . The applied load was measured via the load cell of the test machine, while the displacement of the central roller was measured via a laser extensometer. The specimens were instrumented as sketched in Fig. 8 to confirm the mechanism of collapse: (i) Reflective tabs were adhered to the face sheets directly under the central roller in order to measure the change in the core thickness via a laser extensometer and give the core indentation strain  $\varepsilon_c$ ; (ii) clip gauges were attached at a quarter span on both sides of the central roller to measure the relative sliding displacement of the face sheets and thereby give the average shear strain  $\gamma_c$  in the core; and (iii)  $120 \Omega$  resistance strain gauges of  $2 \text{ mm}$  length were placed at midspan of the back face to measure the longitudinal strains  $\varepsilon_f$  in the face sheet at midspan. Photographs were taken at regular intervals during the bend tests to image the beam throughout the entire deformation history. It is noted that for the clamped configuration, regions of high stress are likely to be present, adjacent to the supports where the filled cells transition to the unfilled cells. However, no instrumentation to measure strains was placed near the clamped supports since (a) no failure was observed in this area in any of the beam tested and (b) the strains near the supports are likely to be strongly dependent on the precise nature of the clamping conditions and hence unlikely to provide any useful information with regard to the mode of deformation.

**4.1 Selection of Beam Geometries.** Beam geometries were selected in order to observe as many collapse modes as practically possible. All beams had a span  $\ell=200 \text{ mm}$  and width  $b=35 \text{ mm}$  and comprised the  $\bar{\rho}=0.1$  square honeycomb core with face sheets of thickness in the range  $t_f=0.75\text{--}4 \text{ mm}$  and core thickness in the range  $H=10.5\text{--}60 \text{ mm}$ . The core comprised cell walls of thickness  $t_c=0.35 \text{ mm}$  and a cell size  $L=7.1 \text{ mm}$  so that  $n=5$  walls were present in the width direction of the beams. The simply supported beams had an overhang  $s=25 \text{ mm}$  in all cases.

The eight geometries employed are labeled A–H and are detailed in Table 2; the predicted failure mode for each is included in Fig. 7. Most of the geometries lie in the core shear and core indentation regimes, with geometries C and D lying at the boundary of the indentation and face microbuckling regimes for the simply supported beams. It was not practical to construct sandwich beams with sufficiently low values of  $H/\ell$  and  $t/H$  in order for face wrinkling to occur.

**4.2 Results.** The test results for geometries A, C, and H are now given in some detail in order to exemplify the three observed collapse modes: core shear, face microbuckling, and core indentation. The measured strengths of all the beams are then compared with the analytical predictions.

*Geometry A.* Recall that the maps of Fig. 7 predict that geometry A fails by core shear for both support conditions. The measured load  $F$  versus displacement  $\delta$  of the central roller for the simply supported and clamped beams of geometry A are plotted in Figs. 9(a) and 9(b), respectively. Following an initial linear response, both beams display a peak load. Subsequently, the load carrying capacity of the simply supported beam reduces monotonically, while the clamped beams display a mildly hardening response up to  $\delta \approx 2.5 \text{ mm}$ . The corresponding measurements of  $\gamma_c$ ,  $\varepsilon_c$ , and  $\varepsilon_f$  are included in Figs. 10(a) and 10(b) for the simply supported and clamped beams, respectively. All measured strains increase gradually up to the peak load, but subsequently  $\gamma_c$  increases sharply for both the clamped and simply supported beams, suggesting that core shear is the failure mode of these beams. This observation is further confirmed from the photographs of the simply supported and clamped beams (Figs. 11(a) and 12(a), respectively) taken after the peak load has been attained. These photographs clearly show shear deformations within the core. The failure mode taking place within the composite core material was matrix shear.

Note that the load carrying capacity of the simply supported beams is significantly diminished after failure of the core while the clamped beams display mild hardening: In the clamped case, axial stretching of the face sheets dominates with increasing  $\delta$ . Hence, membrane stresses play an important role in the post-initial failure load-displacement response of the clamped beams.

*Geometry C.* The maps (Fig. 7) suggest that the simply supported beams fail by a combination of indentation/face microbuckling, while the clamped beams fail by a combined core shear and core indentation. The measured load versus displacement responses are given in Figs. 9(c) and 9(d): Failure is catastrophic with a sudden drop in the load for both types of support. This suggests that the operative failure mechanisms are different from the more benign core shear response of Figs. 9(a) and 9(b). For the clamped beam of geometry C, failure is accompanied by a sudden rise in  $\varepsilon_c$  (see Fig. 10(d)), and this implies that core indentation is triggered. Core indentation is also evident in the photograph of the deformed beam in Fig. 12(b). In contrast, the failure mode of the simply supported beam of geometry C is evident neither from the measurements of  $\gamma_c$ ,  $\varepsilon_c$ , and  $\varepsilon_f$ , as reported in Fig. 10(c), nor from the photograph of the deformed specimen in Fig. 11(b). However, post-failure examination of the specimen

**Table 2 Geometric details of the eight sandwich beam geometries tested in this study. All beams had a span  $\ell=200 \text{ mm}$ , width  $b=35 \text{ mm}$ , and a  $\bar{\rho}=0.1$  square honeycomb core of cell size  $L=7 \text{ mm}$  and web thickness  $t_c=0.35 \text{ mm}$  with  $n=5$  webs across the width of the beam.**

	Specimen label							
	A	B	C	D	E	F	G	H
$t \text{ (mm)}$	4	2	1	0.75	0.75	0.75	0.75	0.75
Number of plies in face sheets	$m_0$	8	4	2	2	2	2	2
$H \text{ (mm)}$	$m_{90}$	8	4	2	1	1	1	1
	10.65	10.65	10.65	10.65	14.20	22.50	37.50	60

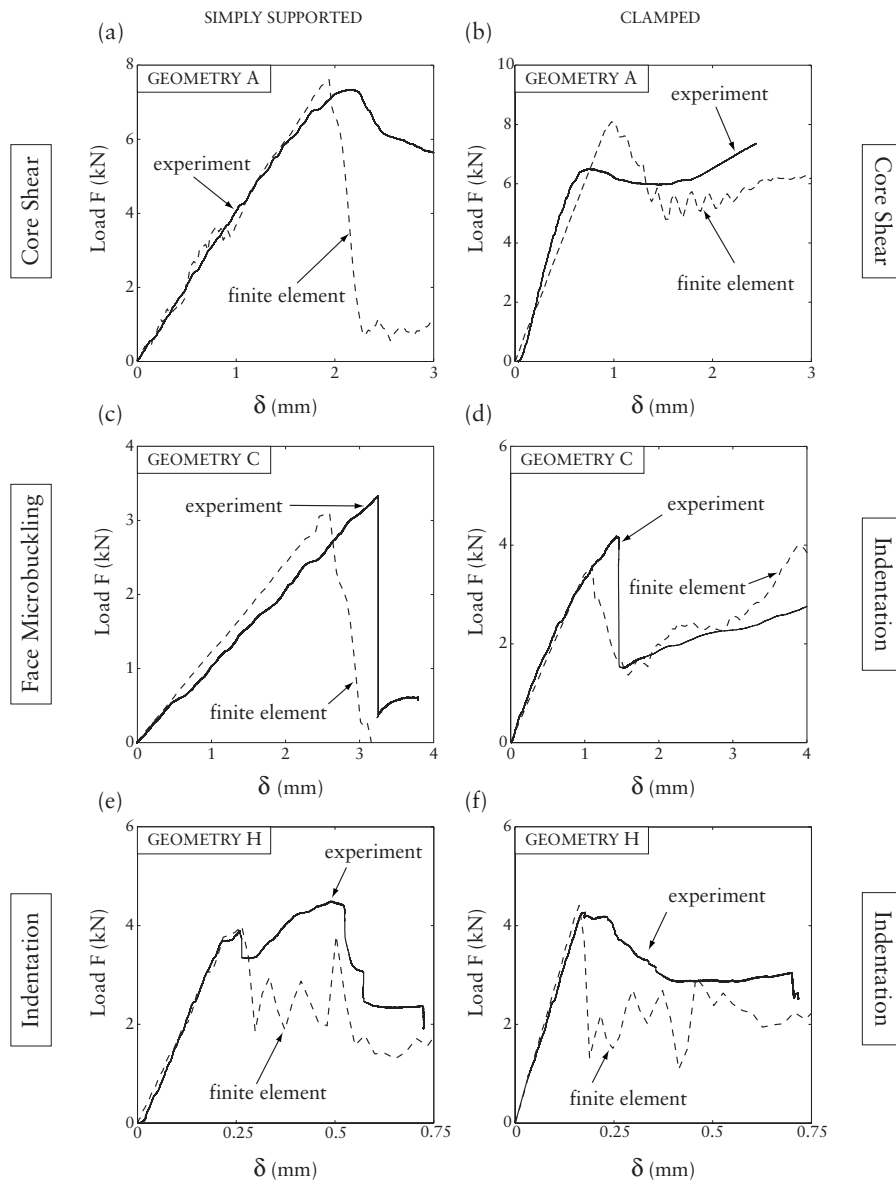


**Fig. 9 The measured load versus displacement curves for three selected geometries A, C, and H. The simply supported beams are (a), (c), and (e), while the clamped geometries are (b), (d), and (f). The corresponding FE predictions along with the observed and predicted collapse modes are also included.**

revealed that microbuckling occurred on the top face sheet directly beneath the roller. The finite element calculations presented subsequently confirm that the simply supported beams fail by microbuckling of the top face sheet: This failure results in a loss of load carrying capacity of the face sheets and thereby to a dramatic load drop as measured in the experiments.

**Geometry H.** The maps (Fig. 7) indicate that both the simply supported and clamped beams fail by core indentation. Similar to geometry A, the simply supported and clamped beams of geometry H display a progressive load drop at failure (Figs. 9(e) and 9(f), respectively). This failure is due to the indentation of the core for both the simply supported and clamped beams, as confirmed by the dramatic increase in  $\varepsilon_c$  after the peak load has been attained (Fig. 10) and also from the photographs of the deformed beams in Figs. 11 and 12. The material failure mode in the indentation region immediately under the indenter is fiber fracture resulting from buckling of the webs of the square honeycomb. Damage to the face sheet under the indenter occurs after the initial damage to

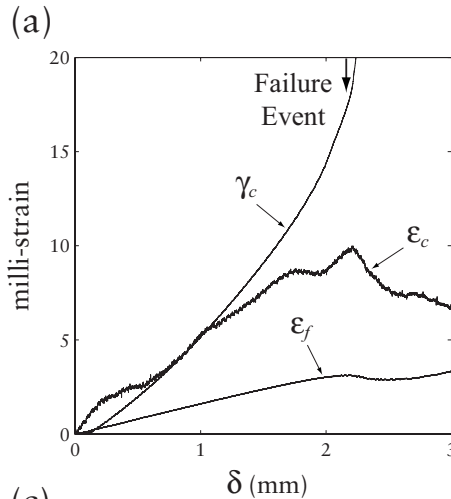
the core; this is clearly seen in the FE calculations (Fig. 14(c)) where the face sheet remains undamaged while significant core indentation is seen. Core indentation results in a reduction in the load carrying capacity of the sandwich beam due to the reduction in the second moment of the area of the sandwich beam cross-section.

The observed failure modes of all beams investigated in this study are listed in Table 3 for the simply supported and clamped beams, respectively, along with the measured peak loads. The analytical predictions of failure mode and collapse load are included. In general, excellent agreement is obtained between the predicted and observed collapse mechanisms and also between the predicted and observed failure loads. The clamped geometry H is the exception: We shall use finite element calculations to understand the source of this discrepancy. It is worth noting here that the analytical predictions of the beam stiffness are in excellent agreement with the measurements for all beams tested in this study.

GEOMETRY A

Core Shear

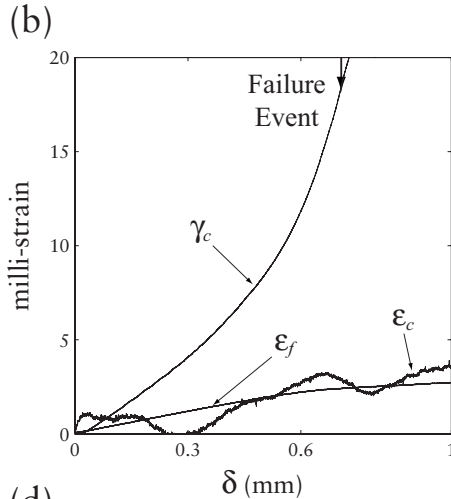
SIMPLY SUPPORTED



GEOMETRY C

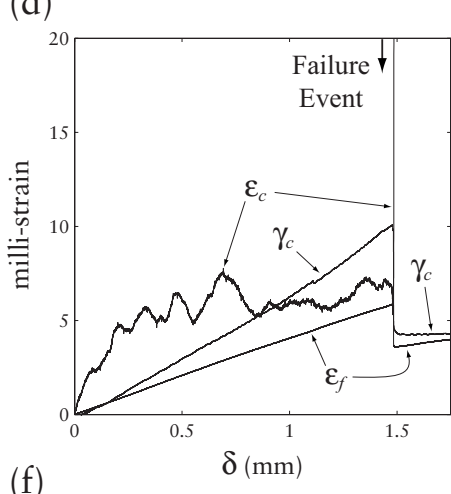
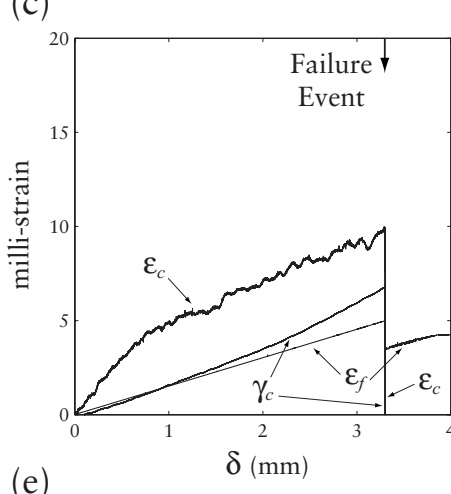
Face Microbuckling

CLAMPED



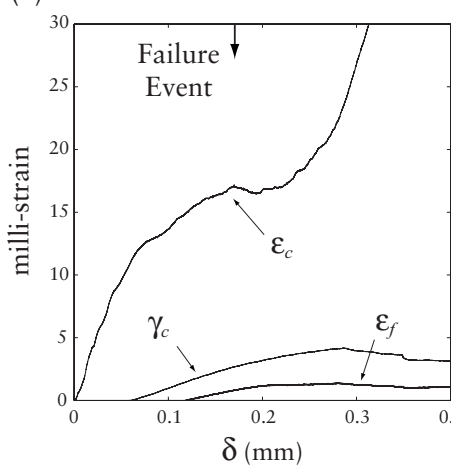
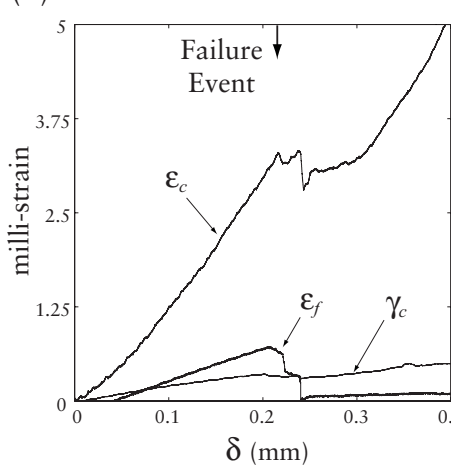
GEOMETRY H

Indentation



Core Shear

Indentation



Indentation

**Fig. 10** The measured (i) core compression  $\epsilon_c$ , (ii) core shear strain  $\gamma_c$ , and (iii) face-sheet strain  $\epsilon_f$  for three selected geometries A, C, and H. The simply supported beams are (a), (c), and (e), while the clamped geometries are (b), (d), and (f).

## 5 Finite Element Calculations

We now report FE calculations of the bending response of the composite square honeycomb core sandwich beams. The main aims of these calculations are to

- investigate the ability of the constitutive model of Matzenmiller et al. [24] and Hashin [25] for fiber composites, as implemented in the commercial finite element code

ABAQUS, to capture the observed collapse modes and measured load versus displacement responses of the composite sandwich beams

- improve the understanding of the deformation and damage modes in the composite sandwich beams

**5.1 Brief Description of the Constitutive Model.** Consider a single ply of a fiber reinforced unidirectional laminate, as shown

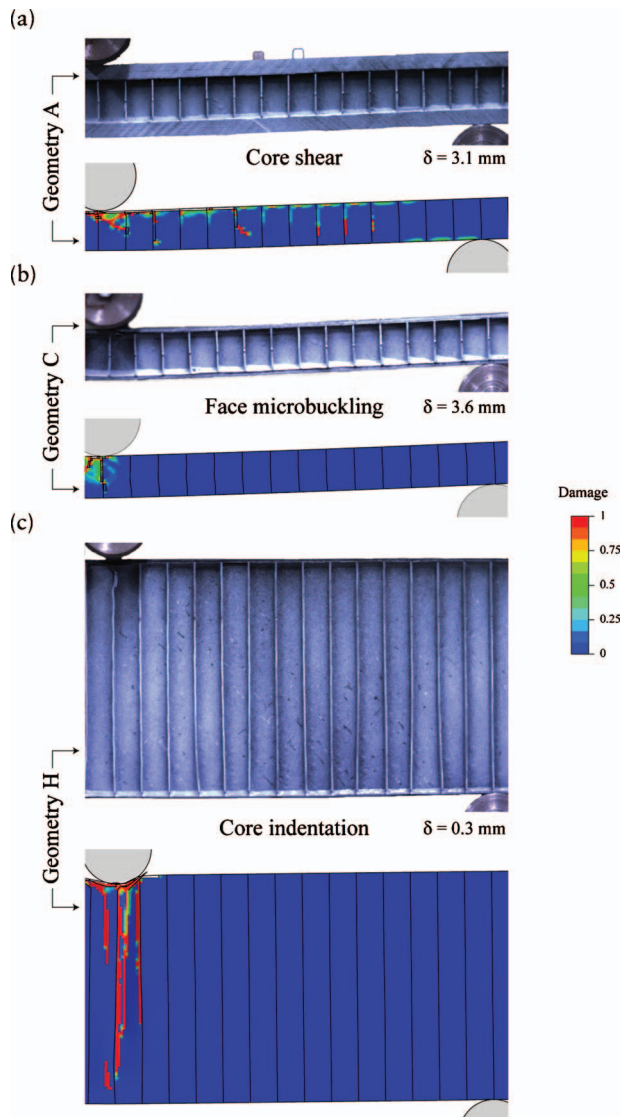


**Fig. 11** Side views of the observed and predicted deformation/failure modes of three selected simply supported beam geometries just after the peak load was attained: (a) geometry A, (b) geometry C, and (c) geometry H. The FE predictions are shaded with contours of the damage variable  $d_s$ , and the beam displacement  $\delta$  for each case is indicated.

in Fig. 13(a), with the  $x_1$  axis in the fiber direction,  $x_2$  in the transverse direction, and  $x_3$  perpendicular to the plane of the ply. The unidirectional ply is transversely isotropic with respect to the fiber direction (i.e.,  $x_1$  axis). For a state of plane stress ( $\sigma_{32} = \sigma_{33} = \sigma_{13} = 0$ ), the elastic response of the *undamaged* material is given by

$$\begin{pmatrix} \varepsilon_{11} \\ \varepsilon_{22} \\ \gamma_{12} \end{pmatrix} = \begin{pmatrix} 1/E_1 & -\nu_{21}/E_1 & 0 \\ -\nu_{12}/E_2 & 1/E_2 & 0 \\ 0 & 0 & 1/G \end{pmatrix} \begin{pmatrix} \sigma_{11} \\ \sigma_{22} \\ \sigma_{12} \end{pmatrix} \quad (5.1)$$

where  $\varepsilon_{11}$  and  $\varepsilon_{22}$  are the direct strains in the  $x_1$  and  $x_2$  directions, respectively, while  $\gamma_{12}$  is the engineering shear strain. The Young's moduli  $E_1$  and  $E_2$  in the  $x_1$  and  $x_2$  directions, along with the shear modulus  $G$  and Poisson's ratios  $\nu_{21}$  and  $\nu_{12}$ , are the five relevant elastic constants of the unidirectional laminate.

**5.1.1 The Damage Law.** The laminate is taken to be linear elastic, as specified by Eq. (5.1), up to the initiation of damage. A nonlinear stress versus strain response accompanies damage pro-

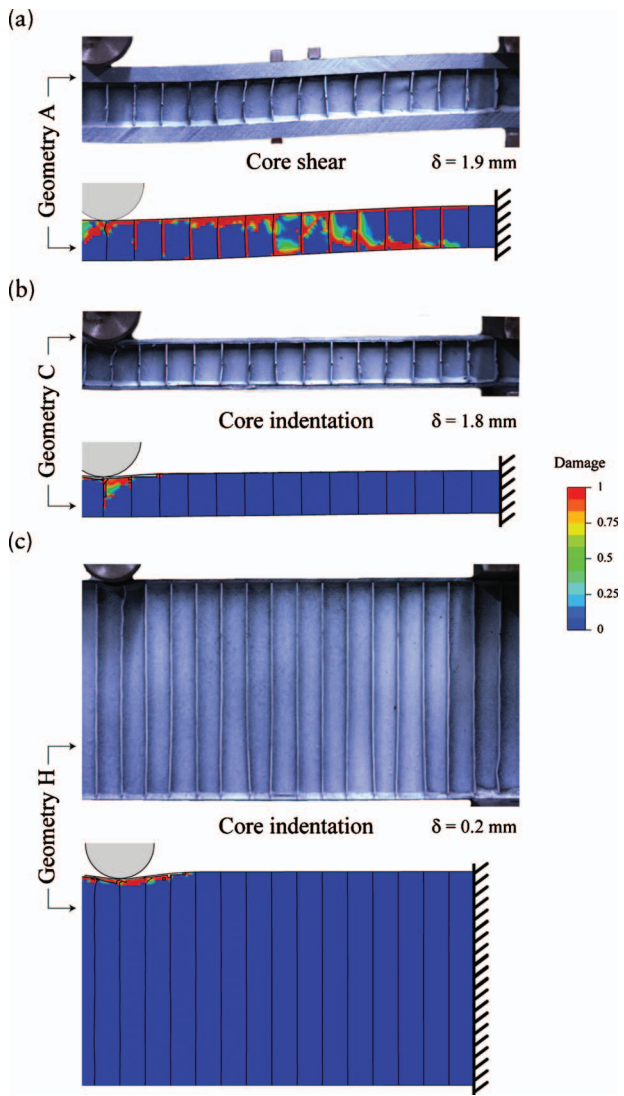


**Fig. 12** Side views of the observed and predicted deformation/failure modes of three selected clamped beam geometries just after the peak load was attained: (a) geometry A, (b) geometry C, and (c) geometry H. The FE predictions are shaded with contours of the damage variable  $d_s$ , and the beam displacement  $\delta$  for each case is indicated.

gression due to a progressive drop in the three moduli ( $E_1, E_2, G$ ) with increasing strain. Four scalar damage variables are introduced, corresponding to four damage modes (tensile and compressive failure in each of the fiber and transverse directions). In the undamaged state, each damage variable is set to zero. As strain-controlled damage accumulates, one or more damage variables increase to a maximum value of unity. The moduli drop with increasing value of the damage variables (Fig. 13(b)), such that one or more moduli equal zero when one of the damage variables attains unity. The damage evolution law follows that laid down by Matzenmiller et al. [24]. A full description of the damage model is given in the Appendix.

**5.2 Calibration of Material Parameters.** We now calibrate the material parameters in the constitutive model for the laminate and woven materials using data from the tensile and compressive material tests reported in Sec. 2.3. Readers are referred to the Appendix for a description of the parameters of the damage model.

*Face-sheet laminate.* The elastic moduli follow directly from

**Table 3 Comparison of the experimentally observed (EX) collapse modes and peak loads as in the experiments with the analytical (AN) and finite element (FE) predictions for (a) the simply supported and (b) clamped beams. The collapse modes are labeled as (i) core shear (CS), (ii) face microbuckling (FM), and (iii) core indentation (CI).**

Geometry	Collapse mode			Peak load (kN)			Stiffness $F/\delta$ (kN/mm)				
	EX	FE	AN	EX	FE	AN	EX	FE	AN		
(a) Simply supported	A	CS	CS	CS	7.3	7.5	6.4	4.1	4.0	4.3	
	B	CS	FM	CS	5.8	5.3	5.4	2.0	2.2	2.2	
	C	FM	FM	CS/FM/CI		3.3	3.3	4.4	1.0	1.2	1.1
	D	CI	FM/CI	FM/CI		3.6	2.9	3.3	0.9	1.2	0.8
	E	CI	FM/CI	CI		3.3	3.5	3.6	1.5	2.0	1.3
	F	CI	CI	CI		4.6	3.8	4.1	3.0	4.7	3.1
	G	CI	CI	CI		4.7	4.0	4.9	9.4	9.8	7.6
	H	CI	CI	CI		4.5	4.3	5.7	17.4	17.4	17.1
(b) Clamped	A	CS	CS	CS	6.5	8.4	6.4	10.8	8.6	7.5	
	B	CS	CS/CI		5.6	5.7	5.4	6.0	5.5	5.3	
	C	CI	CI	CS/CI		4.2	3.8	4.8	3.8	3.4	3.3
	D	CI	CI	CS/CI		3.9	3.5	4.1	3.6	3.4	2.6
	E	CI	CI	CI		3.9	3.9	4.5	6.8	5.3	4.2
	F	CI	CI	CI		4.2	4.2	5.2	8.8	10.4	8.6
	G	CI	CI	CI		4.1	4.2	6.2	19.2	19.3	18.5
	H	CI	CI	CI		4.3	4.2	7.2	25.4	27.4	35.8

the tensile tests on the laminates in the 0–90 deg and ±45 deg orientations. Neglecting the contribution from the 90 deg ply, the modulus is  $E_1=2E_l^0=170$  GPa, with the strain gauge measurements giving the Poisson's ratio as  $\nu_{12}=\nu_{21}=0.15$ . In order to determine the in-plane shear modulus  $G$  of the material, consider the tension test on the laminate in the ±45 deg orientation. Write the applied tensile stress as  $\sigma_x$  and the corresponding axial and transverse strains as  $\varepsilon_x$  and  $\varepsilon_y$ , respectively. Then, the required shear stress  $\tau$  versus shear strain  $\gamma$  relation is obtained via the connections  $\tau=\sigma_x/2$  and  $\gamma=\varepsilon_x-\varepsilon_y$ . The shear modulus  $G=4.7$  GPa follows immediately as the initial slope of the  $\tau$  versus  $\gamma$ . Some additional tensile tests were conducted on a single ply of the laminate in the 90 deg orientation (i.e., fibers perpendicular to the tensile direction) to give the modulus  $E_2=5.1$  GPa. The tensile and compressive strengths in the fiber direction follow from the tension and compression tests in 0–90 deg orientation as  $X^T=2\sigma_l^{0T}=1960$  MPa and  $X^C=2\sigma_l^{0C}=1260$  MPa, where again we neglect the contribution from the 90 deg ply. The transverse strength  $Y$  is essentially that of the matrix. Thus, assuming an isotropic response of the matrix, tensile tests in the ±45 deg orientation give  $Y=160$  MPa.

Recall that in the 0–90 deg orientation, the composite fails immediately after the peak stress has been attained. We thus set the fiber fracture energies as  $J_f^t/L_e=\alpha(X^T)^2/E_1$  and  $J_f^c/L_e=\alpha(X^C)^2/E_1$ , while the matrix fracture energy is given as  $J_m/L_e=Y\bar{\varepsilon}/2$ , where  $\bar{\varepsilon}=0.12$  is the tensile fracture strain of the laminate in the ±45 deg orientation. The coefficient  $\alpha$  dictates the rate of

softening of the damage part of the stress-strain response. A value of  $\alpha=0.5$  would imply an immediate transition from the initiation of damage to the fully damaged state; hence, a value of  $\alpha=0.6$  is chosen to be large enough to aid numerical convergence but small to reflect the diminutive fraction of energy absorbed after peak-spot checks confirmed that the results are not sensitive to the choice of  $\alpha$  in the range 0.55–0.75.

*Woven core material.* The woven composite comprises two sets of orthogonal fibers in a single ply. To model this within the above described constitutive framework, which models unidirectional plies, we assume that each woven layer comprises two unidirectional fiber plies stacked so that the fibers in the two plies are orthogonal to each other. Each of these plies has half the thickness of the thickness  $t_c$  of the woven composite material. We now specify the properties for these virtual unidirectional fiber plies of the woven material.

The elastic modulus  $E_1=2E_w^0=126$  GPa and Poisson's ratio  $\nu_{21}=\nu_{12}=0.2$  were measured from the tensile tests on the woven material in the 0–90 deg orientation, while the shear modulus  $G=4.7$  GPa was inferred from the tensile test in the ±45 deg orientation as described above. It is not possible to conduct a tensile/compressive test to deduce the properties of the virtual unidirectional ply of the woven material in the transverse direction ( $x_2$  direction). However, it is clear that the properties in the  $x_2$  direction are dominated by the matrix, and hence we set the modulus  $E_2$  equal to that of the laminate material described above, i.e.,  $E_2=5.1$  GPa. The tensile and compressive strengths in the fiber

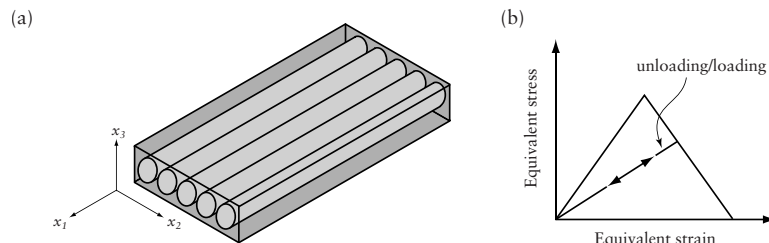


**Fig. 13 (a)** Sketch illustrating the coordinate system for a single ply of a unidirectional laminate and (b) the assumed equivalent stress versus strain relationship for each of the four damage modes. Unloading from a damaged state occurs linearly toward the origin, as shown in (b).

**Table 4** The material properties of each unidirectional ply of the woven and laminate composite materials employed in the constitutive model in the FE calculations

Material	Property	Value
Woven	$E_1$ (GPa)	126
	$E_2$ (GPa)	5.1
	$G$ (GPa)	4.7
	$\nu_{12} = \nu_{21}$	0.2
	$X^T$ (MPa)	1080
	$X^C$ (MPa)	660
	$Y$ (MPa)	160
	$J_f^t/L_e$ (MPa)	5.6
	$J_f^c/L_e$ (MPa)	2.1
	$J_m/L_e$ (MPa)	9.6
	Ply thickness (mm)	0.175
	Density (kg m <sup>-3</sup> )	1370
Laminate	$E_1$ (GPa)	170
	$E_2$ (GPa)	5.1
	$G$ (GPa)	4.7
	$\nu_{12} = \nu_{21}$	0.15
	$X^T$ (MPa)	1960
	$X^C$ (MPa)	1260
	$Y$ (MPa)	160
	$J_f^t/L_e$ (MPa)	13.6
	$J_f^c/L_e$ (MPa)	5.6
	$J_m/L_e$ (MPa)	9.6
	Ply thickness (mm)	0.25
	Density (kg m <sup>-3</sup> )	1570

direction are extracted from the tests in the 0–90 deg orientation as  $X^T=2\sigma_w^{0t}=1080$  MPa and  $X^C=2\sigma_w^{0c}=660$  MPa. Again, it is not possible to directly measure the transverse strength  $Y$ , which is dominated by the strength of the matrix. Hence, we use  $Y=160$  MPa, i.e., equal to that of the laminate material.

Similar to the laminate material, the fiber fracture energies were taken to be  $J_f^t/L_e=\alpha(X^T)^2/E_1$  and  $J_f^c/L_e=\alpha(X^C)^2/E_1$ , while the matrix fracture energy  $J_m/L_e$  was set equal to that of the laminate material. Again, the coefficient  $\alpha=0.6$ .

The material properties of a single ply of the laminate and woven materials to be used in the constitutive model are listed in Table 4. In order to judge the suitability of these parameters, we present predictions of tensile and compressive responses of the laminate and woven materials corresponding to the experiments discussed in Sec. 2.3. Thus, both the laminate and woven materials were modeled as comprising two orthogonal plies, with each ply assigned the properties listed in Table 4. The predictions of the tensile/compressive responses for the laminate and woven materials are included in Figs. 3(a) and 3(b), respectively, for both the 0–90 deg and ±45 deg orientations. The agreement with measurements for the 0–90 deg orientation is excellent in terms of the modulus, peak strength, and post-peak responses. However, in the ±45 deg orientation, the measured response does not display a linear softening behavior as assumed in the damage evolution laws detailed in Sec. 5.1. Thus, while the model accurately captures the initial elastic response and peak strength, it does not model the entire stress versus strain curve to high fidelity. The consequences of this inaccuracy are discussed while comparing the FE predictions with the beam measurements in Sec. 5.4.

**5.3 Description of the FE Model.** Finite strain three dimensional FE simulations were conducted using the explicit version of the commercial finite element package ABAQUS (version 6.8). The composite sandwich beams were modeled using four-noded shell elements with reduced integration (S4R in the ABAQUS notation). The *composite shell section* option was employed to model the composite sheets comprising a number of plies with unidirectional

fibers in different orientations. Integration through the thickness of the shell was performed using Simpson's rule with three integration points per ply.

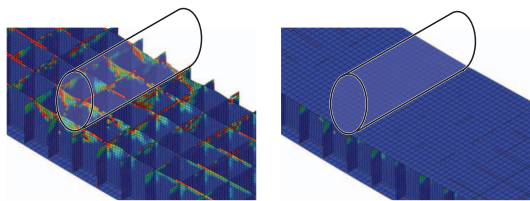
Recall that the sandwich beam face sheets comprised 3–16 plies, depending upon the beam geometry. These plies were oriented as specified in Table 2, and each ply was assigned the properties of the laminate material, as detailed in Sec. 5.2. The webs of the square honeycomb core comprised a single layer of the woven composite material of thickness  $t_c=0.35$  mm, and these were modeled as a pair of orthogonal plies of thickness  $t_c/2$ , as discussed in Sec. 5.2. Each ply was assigned the properties listed in Table 4, and the fibers in each ply were oriented at ±45 deg with respect to the  $x_3$  axis of the beam (Fig. 1(b)). The cell size  $L$ , core height  $H$ , and number of webs of the square honeycomb core matched the test configuration. Ideal bonding was assumed between the core and face sheets, and so the core nodes were tied to the face-sheet nodes. In order to allow for the possibility of buckling, an imperfection was introduced into the core of the sandwich by perturbing the structure using a linear combination of the first 20 elastic eigenmodes. The maximum imperfection amplitude was 2% of the honeycomb wall thickness.

It is necessary to specify the densities of the composite sheets since the calculations were performed using an explicit FE code. Consistent with the measurements, the densities of the core and face-sheet materials were taken as 1370 kg m<sup>-3</sup> and 1570 kg m<sup>-3</sup>, respectively. However, for the applied rates of the loading, inertial effects are negligible, and hence the FE results represent the quasi-static response, independent of inertial effects. The FE mesh comprised approximately square elements of 1.2 mm size in the face sheets and 0.7 mm in the core. The element removal option in ABAQUS was employed: An element was removed from the calculation when all four independent damage variables within that element attain their maximum value of unity, and the element was no longer able to sustain any stress. A mesh sensitivity study was performed to ensure that the finite element meshes were fine enough to give converged results. Note that the calculations display some mesh size sensitivity once damage occurs due to the softening nature of the response. However, this mesh size sensitivity is greatly alleviated by choosing the representative length scale  $L_e$  to equal the characteristic mesh size; i.e.,  $L_e$  is chosen so that the fracture energy per unit area,  $J$ , is related to the failure stress  $\sigma_f$  and the modulus  $E$  via the relation  $J/L_e=\alpha\sigma_f^2/E$ .

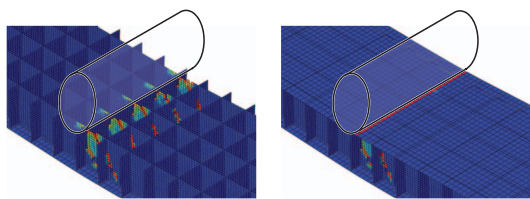
The clamped beams were modeled by fully constraining the nodes on the face sheet and core at both ends of the beam so as to have a beam of span  $\ell=200$  mm. Loading was applied via a rigid cylindrical roller of radius  $R=19$  mm at midspan, as in the experiments. The roller was displaced at a rate of 0.2 mm min<sup>-1</sup>, and the load was determined. Contact between all surfaces in the model was modeled using the general contact option in ABAQUS explicit with a coefficient of friction  $\mu=0.1$  specified for all the surfaces (results are not sensitive to this choice of the value of  $\mu$ , but including some friction increased the stability of the calculations). As in the experiments, the simply supported beams of 250 mm length were supported on cylindrical rollers of radius  $R=19$  mm at the two ends of the beam such that the beam had a central span  $\ell=200$  mm and an overhang  $s=25$  mm beyond each of the outer supporting rollers (Fig. 5(a)). Loading was again applied by displacing the central roller at 0.2 mm min<sup>-1</sup>, and the general contact option was used to model contact between the beam and rollers with  $\mu=0.1$ . The calculations are not sensitive to variations in the friction coefficient over a realistic range 0.1–0.3.

**5.4 Comparison of the FE Predictions and Observations.** Comparisons between the measured and FE predictions of the load versus displacement responses of the clamped and simply supported beams of geometries A, C, and H are included in Fig. 9. The serrations in the predicted load versus displacement curves are due to the successive failure of elements.

(a) Core shear - Geometry A



(b) Face microbuckling - Geometry C



(c) Core indentation - Geometry H

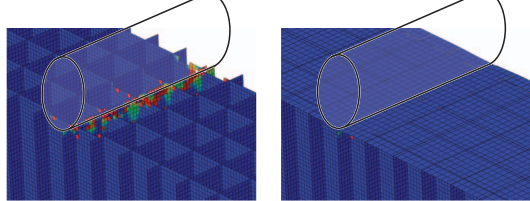


**Fig. 14** Images showing the FE predictions of damage  $d_s$  just after the peak load has been attained in selected simply supported sandwich beams: (a) geometry A, (b) geometry C, and (c) geometry H. The roller is included to better illustrate the locations of the damage, and images with both the top face sheet present and absent are included so as to visualize the face sheet and core damage clearly.

Good agreement is obtained in all cases for the peak load, but the post-peak response is not accurately captured for the simply supported geometry A beam. This beam fails by core shear, and the FE model predicts a dramatic load drop, while the measured response is much more benign. The precise reasons for this discrepancy are unclear but might be related to the FE model not accurately computing the shearing of the redux glue used to bond the core to the face sheets.

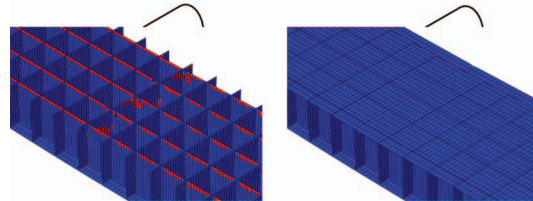
The predicted damage  $d_s$  near the midspan of beams A, C, and H are shown in Figs. 14 and 15 for the simply supported and clamped beams, respectively. Recall that the damage parameter  $d_s$  indicates damage by any of the four modes. The figures show the deformed beams just after the peak load had been attained with the top face sheet removed (in order to better visualize the core damage) and with the top face sheet present in each case. From these figures, we infer the following for the simply supported beams:

- (i) geometry A: extensive damage in the core over the length of the beam indicative of core shear with no damage in the face sheets
- (ii) geometry C: a clear line of damage in the top face sheet immediately beneath the central roller combined with localized damage in the core under the central indenter (this suggests a combined face microbuckling and core indentation failure mode)
- (iii) geometry H: only localized damage in the core beneath the central indenter, indicating a core indentation failure mode

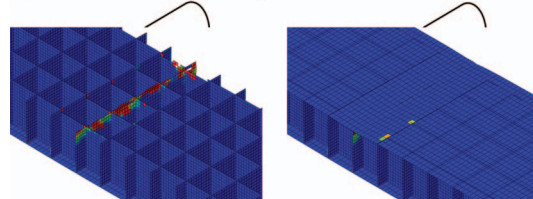
These predictions are consistent with both the experimental observations and the analytical predictions. The corresponding mechanisms for the clamped beams are as follows:

- (i) geometry A: extensive damage in the core over the length

(a) Core shear - Geometry A



(b) Core indentation - Geometry C



(c) Core indentation - Geometry H

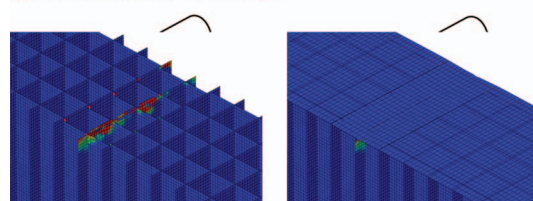


**Fig. 15** Images showing the FE predictions of damage  $d_s$  just after the peak load has been attained in selected clamped sandwich beams: (a) geometry A, (b) geometry C, and (c) geometry H. The roller is included to better illustrate the locations of the damage, and images with both the top face sheet present and absent are included so as to visualize the face sheet and core damage clearly.

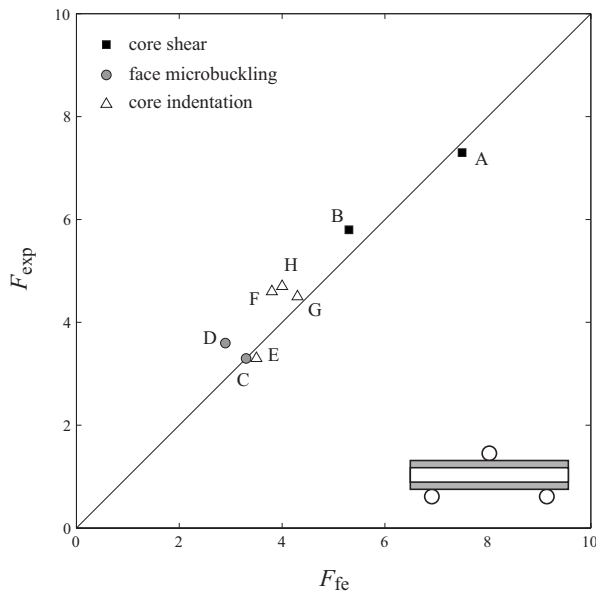
of the beam again indicative of core shear, with no damage in the face sheets

- (ii) geometries C and H: damage in the core immediately beneath the central roller indicative of core indentation

Comparisons between measurements of predictions of local strains are included in Fig. 16 for the cases discussed in Fig. 10: For the sake of clarity, only the strains corresponding to the failure mode are included in Fig. 16 as in any case the other strains remain small. Reasonable agreement is seen in most cases with the exceptions of Fig. 16(b)—this discrepancy is attributed to an imperfect clamped boundary condition in the experiment, which permits a larger shear strain. A direct comparison of the predicted damage distribution and the deformed beams is given in Fig. 11 for the three simply supported beams A, C, and H, and likewise for the end-clamped beams in Fig. 12. Contours of the predicted damage  $d_s$  on side views of the beams are set alongside the corresponding photographs taken during the experiments. These side views clearly illustrate that the FE calculations accurately predict the deformation and failure modes.

The FE predictions of the failure mode and peak load for all the simply supported and clamped beams are included in Table 3 along with the corresponding experimental observations and analytical predictions. Again, reasonable agreement between the predictions and observations is noted over the full range of beam geometries and boundary conditions investigated in this study. The main discrepancies are due to the fact that the FE model predicts a softening post-yield tensile response of the composite in the  $\pm 45$  deg orientation, while measurements (Fig. 3) display a mildly hardening response. This discrepancy is due to the damage law that exists in the ABAQUS implementation of the Matzenmiller–Hashin damage mode. This experimental study has

(a)



(b)

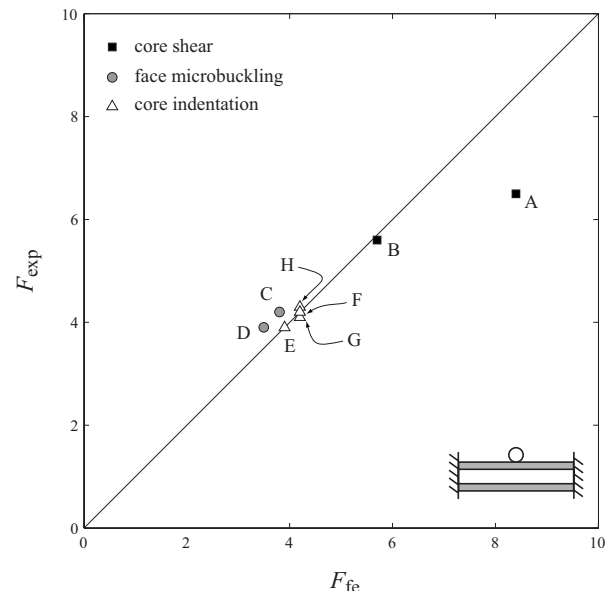


**Fig. 16 Comparison of measured and finite element calculations for selected strains: (i) core compression  $\varepsilon_c$ , (ii) core shear strain  $\gamma_c$ , and (iii) face-sheet strain  $\varepsilon_f$  for three selected geometries A, C, and H. The simply supported beams are (a), (c), and (e), while the clamped geometries are (b), (d), and (f).**

highlighted this critical deficiency in using this model for making structural predictions.

## 6 Concluding Remarks

Eight geometries of composite sandwich beams with square honeycomb cores have been manufactured from carbon fiber composite sheets and tested in three-point bending in both the simply supported and clamped configurations. Analytical models are reported for the collapse loads by four mechanisms: (i) face microbuckling, (ii) core shear, (iii) core indentation, and (iv) face wrinkling. The eight geometries of the sandwich beams were designed to demonstrate the first three of these collapse mechanisms. The main aim of the analytical modeling was to aid geometry design in experiments and, as such, was not expected to yield accurate predictions of the failure loads. Nevertheless, good agreement was observed between the predictions and measurements of peak load over most geometries, and the model coped very well in predicting the observed collapse mechanisms.

To date, there has been little or no measurement or modeling of composite sandwich beams incorporating composite lattice cores. This paper presents a thorough characterization of a novel lattice material in a beam configuration, exploring the failure mechanics of these structures as well as their mechanical response. A second significant outcome from this work is the success in employing relatively simple FE calculations to a complex material and geometry system.

The constitutive model of Matzenmiller et al. [24] and Hashin [25] for the initiation and development of damage in unidirectional fiber composites was calibrated against tensile and compressive tests on the composite material sheets. Some key discrepancies between the model as implemented in ABAQUS and measurements were noted, especially with regard to loading at 45 deg to the fiber direction. A finite element model was constructed by treating the sandwich beams as an assembly of unidirectional plies, with fibers in the appropriate orientation. The 3D beam geometry, with all the geometrical details of the honeycomb core and face sheet, was modeled, and perfect bonding was assumed between core and face sheets. The FE calculations, in general,

accurately captured both the measured load versus displacement responses and the observed deformation and failure modes. The modeling of the response following failure of the beam shows a number of significant differences to the experiment. This limitation is due to the simplicity of the material model (particularly at 45 deg angle to the fiber directions). However, it is concluded that the relatively simple fiber composite constitutive framework is adequate for the modeling of the composite sandwich structures insomuch as predicting the onset of damage, the failure mechanisms, and the peak loadings considered herein.

## Acknowledgment

The authors acknowledge support from the Office of Naval Research (ONR) via Grant No. N00014-09-1-0573 and from the Engineering and Physical Sciences Research Council, UK (EPSRC).

## Appendix: Brief Description of the Laminate Damage Model

The damage model comprises two steps. First, damage can accumulate when a critical strain state is attained, as proposed by Hashin [25], and this condition is usually re-expressed in terms of the associated critical stress state. This is similar to the yield surface in plasticity theory: For a stress state within the damage locus, no additional damage occurs, and the stress versus strain response is linear and reversible. Second, the damage variable(s) increase nonlinearly with increasing strain, and this leads to a drop in moduli and thereby to a drop in stress. The damage evolution law follows that laid down by Matzenmiller et al. [24]. A full description of the damage model is given in the Appendix.

We denote the tensile and compressive strengths for damage initiation in the undamaged laminate and in the fiber direction ( $x_1$ -direction) by  $X^T$  and  $X^C$ , respectively. The corresponding tensile and compressive strengths in the transverse direction are denoted by  $Y$ . After damage has developed, these strengths drop as follows. Write the damage variable for the tensile failure in the fiber direction as  $d_f$ . Then, the current tensile strength in the fiber direction is  $(1-d_f)X^T$ . Likewise, the damage variable for com-

pressive loading in the fiber direction is  $d_f^c$ , while those for transverse tension and compression are  $d_m^t$  and  $d_m^c$ , respectively. No additional damage develops when the stress state lies within the following critical surfaces:

$$\frac{\langle \sigma_{11} \rangle}{(1 - d_f^t)X^T} < 1 \quad (\text{A1})$$

$$\frac{\langle -\sigma_{11} \rangle}{(1 - d_f^c)X^c} < 1 \quad (\text{A2})$$

$$\left( \frac{\langle \sigma_{22} \rangle}{(1 - d_m^t)Y} \right)^2 + \left( \frac{2\sigma_{12}}{(1 - d_s)Y} \right)^2 < 1 \quad (\text{A3})$$

and

$$\left( \frac{\langle -\sigma_{22} \rangle}{(1 - d_m^c)Y} \right)^2 + \left( \frac{2\sigma_{12}}{(1 - d_s)Y} \right)^2 < 1 \quad (\text{A4})$$

where  $\langle \cdot \rangle$  represents the Macaulay bracket of value zero when its argument is negative. The shear damage  $d_s$  is defined as

$$d_s = 1 - (1 - d_f^t)(1 - d_f^c)(1 - d_m^t)(1 - d_m^c) \quad (\text{A5})$$

In any given state of damage, the secant relationship between stress and strain reads

$$\begin{pmatrix} \varepsilon_{11} \\ \varepsilon_{22} \\ \gamma_{12} \end{pmatrix} = \begin{pmatrix} 1/[E_1(1 - d_f)] & -\nu_{12}/[E_1(1 - d_f)] & 0 \\ -\nu_{12}/[E_2(1 - d_m)] & 1/[E_2(1 - d_m)] & 0 \\ 0 & 0 & 1/[G(1 - d_s)] \end{pmatrix} \times \begin{pmatrix} \sigma_{11} \\ \sigma_{22} \\ \sigma_{12} \end{pmatrix} \quad (\text{A6})$$

where

$$d_f = \begin{cases} d_f^t & \text{if } \sigma_{11} \geq 0 \\ d_f^c & \text{otherwise} \end{cases}$$

and

$$d_m = \begin{cases} d_m^t & \text{if } \sigma_{22} \geq 0 \\ d_m^c & \text{otherwise} \end{cases} \quad (\text{A7})$$

We note from Eqs. (A7) and (A8) that if the composite is fully damaged in, say, the compressive fiber damage mode, it can still sustain tensile fiber stresses. The validity of this assumption remains to be verified experimentally.

The evolution law is now summarized for each of the four independent damage variables  $d_f^t$ ,  $d_f^c$ ,  $d_m^t$ , and  $d_m^c$ . The damage growth law adopted here is based upon the assumption that the stress decreases linearly with increasing strain once damage initiates. First, consider the tensile fiber damage mode. An effective strain  $\hat{\varepsilon}_f^t$  is defined as  $\hat{\varepsilon}_f^t \equiv \langle \varepsilon_{11} \rangle$  and is used to update the damage state variable via the relation

$$d_f^t = \frac{\frac{2J_f^t}{L_e X^T}(\hat{\varepsilon}_f^t - X^T/E_1)}{\hat{\varepsilon}_f^t \left( \frac{2J_f^t}{L_e X^T} - X^T/E_1 \right)} \leq 1 \quad (\text{A8})$$

where  $X^T/E_1$  is the value of  $\hat{\varepsilon}_f^t$  when the tensile fiber first initiates and  $2J_f^t/L_e X^T$  is the strain for a complete tensile fiber damage. Here,  $J_f^t$  is the tensile fiber fracture energy, and  $L_e$  is a representative length scale. We note in passing that an additional constraint must be imposed upon Eq. (A8) for it to be meaningful:  $d_f^t \geq 0$ , reflecting the fact that damage is irreversible. When the axial strain is decreased, we hold  $d_f^t$  fixed.

Similarly, the compressive fiber damage variable is specified as

$$d_f^c = \frac{\frac{2J_f^c}{L_e X^c}(\hat{\varepsilon}_f^c - X^c/E_1)}{\hat{\varepsilon}_f^c \left( \frac{2J_f^c}{L_e X^c} - X^c/E_1 \right)} \leq 1 \quad (\text{A9})$$

where  $J_f^c$  is the compressive fiber fracture energy and the effective strain is  $\hat{\varepsilon}_f^c \equiv \langle -\varepsilon_{11} \rangle$ . The matrix damage variables are given by

$$d_m^t = \frac{\frac{2J_m}{L_e Y}(\hat{\varepsilon}_m^t - Y/E_2)}{\hat{\varepsilon}_m^t \left( \frac{2J_m}{L_e Y} - Y/E_2 \right)} \leq 1 \quad (\text{A10})$$

and

$$d_m^c = \frac{\frac{2J_m}{L_e Y}(\hat{\varepsilon}_m^c - Y/E_2)}{\hat{\varepsilon}_m^c \left( \frac{2J_m}{L_e Y} - Y/E_2 \right)} \leq 1 \quad (\text{A11})$$

where  $J_m$  is the matrix fracture energy and the effective strains are defined as  $\hat{\varepsilon}_m^t \equiv \sqrt{\langle \varepsilon_{22} \rangle^2 + \varepsilon_{12}^2}$  and  $\hat{\varepsilon}_m^c \equiv \sqrt{\langle -\varepsilon_{22} \rangle^2 + \varepsilon_{12}^2}$ . In this study, we choose  $L_e$  to be the size of a finite element; numerical experimentation confirmed that this choice gives a response that is almost independent of mesh size.

## References

- [1] Ashby, M. F., Evans, A. G., Fleck, N. A., Gibson, L. J., Hutchinson, J. W., and Wadley, H. N. G., 2000, *Metal Foams: A Design Guide*, Butterworth-Heinemann, Boston, MA.
- [2] Deshpande, V. S., Ashby, M. F., and Fleck, N. A., 2001, "Foam Topology Bending Versus Stretching Dominated Architectures," *Acta Mater.*, **49**(6), pp. 1035–1040.
- [3] Gibson, L. J., and Ashby, M. F., 1997, *Cellular Solids, Structure and Properties*, 2nd ed., Cambridge University Press, Cambridge, UK.
- [4] Wadley, H. N. G., Fleck, N. A., and Evans, A. G., 2003, "Fabrication and Structural Performance of Periodic Cellular Metal Sandwich Structures," *Compos. Sci. Technol.*, **63**(16), pp. 2331–2343.
- [5] Côté, F., Deshpande, V. S., Fleck, N. A., and Evans, A. G., 2004, "The Out-of-Plane Compressive Behavior of Metallic Honeycombs," *Mater. Sci. Eng., A*, **380**(1–2), pp. 272–280.
- [6] Côté, F., Deshpande, V. S., Fleck, N. A., and Evans, A. G., 2006, "The Compressive and Shear Responses of Corrugated and Diamond Lattice Materials," *Int. J. Solids Struct.*, **43**(20), pp. 6220–6242.
- [7] Finnegan, K., Kooistra, G., Wadley, H. N. G., and Deshpande, V. S., 2007, "The Compressive Response of Carbon Fiber Composite Pyramidal Truss Sandwich Cores," *Int. J. Mater. Res.*, **98**(12), pp. 1264–1272.
- [8] Russell, B. P., Deshpande, V. S., and Wadley, H. N. G., 2008, "Quasistatic Deformation and Failure Modes of Composite Square Honeycombs," *J. Mech. Mater. Struct.*, **3**(7), pp. 1315–1340.
- [9] Kazemahvazi, S., and Zenkert, D., 2009, "Corrugated All-Composite Sandwich Structures. Part 1: Modeling," *Compos. Sci. Technol.*, **69**(7–8), pp. 913–919.
- [10] Kazemahvazi, S., Tanner, D., and Zenkert, D., 2009, "Corrugated All-Composite Sandwich Structures. Part 2: Failure Mechanisms and Experimental Programme," *Compos. Sci. Technol.*, **69**(7–8), pp. 920–925.
- [11] Zenkert, D., 1996, *An Introduction to Sandwich Construction*, Chameleon, London, UK.
- [12] Plantema, F. J., 1966, *Sandwich Construction*, Wiley, New York.
- [13] Allen, H. G., 1969, *Analysis and Design of Structural Sandwich Panels*, Pergamon, Oxford, UK.
- [14] Chen, C., Harte, A. M., and Fleck, N. A., 2001, "The Plastic Collapse of Sandwich Beams With a Metallic Foam Core," *Int. J. Mech. Sci.*, **43**(6), pp. 1483–1506.
- [15] McCormack, T. M., Miller, R., Kesler, O., and Gibson, L. J., 2001, "Failure of Sandwich Beams With Metallic Foam Cores," *Int. J. Solids Struct.*, **38**(28–29), pp. 4901–4920.
- [16] Petras, A., and Sutcliffe, M. P. F., 1999, "Failure Mode Maps for Honeycomb Sandwich Panels," *Compos. Struct.*, **44**(4), pp. 237–252.
- [17] Shenhav, Y., Frostig, Y., and Altus, E., 1996, "Stresses and Failure Patterns in the Bending of Sandwich Beams With Transversely Flexible Cores and Laminated Composite Skins," *Compos. Struct.*, **35**(2), pp. 143–152.
- [18] Frostig, Y., Baruch, M., Vilnay, O., and Sheinman, I., 1992, "High-Order Theory for Sandwich-Beam Behavior With Transversely Flexible Core," *J. Eng. Mech.*, **118**(5), pp. 1026–1043.
- [19] Frostig, Y., and Baruch, M., 1993, "High-Order Buckling Analysis of Sandwich Beams With Transversely Flexible Core," *J. Eng. Mech.*, **119**(3), pp. 476–495.

- [20] Steeves, C. A., and Fleck, N. A., 2004, "Collapse Mechanisms of Sandwich Beams With Composite Faces and a Foam Core, Loaded in Three-Point Bending. Part I: Analytical Models and Minimum Weight Design," *Int. J. Mech. Sci.*, **46**(4), pp. 561–583.
- [21] Tagarielli, V. L., Fleck, N. A., and Deshpande, V. S., 2004, "Collapse of Clamped and Simply Supported Composite Sandwich Beams in Three-Point Bending," *Composites, Part B*, **35**(6–8), pp. 523–534.
- [22] Daniel, I. M., and Gdoutos, E. E., 2009, "Failure Modes of Composite Sandwich Beams," *Major Accomplishments in Composite Materials and Sandwich Structures*, Springerlink, New York.
- [23] Daniel, I. M., Rajapakse, Y. D. S., and Gdoutos, E. E., eds., 2009, *Major Accomplishments in Composite Materials and Sandwich Structures*, Springer, New York.
- [24] Matzenmiller, A., Lubliner, J., and Taylor, R. L., 1995, "A Constitutive Model for Anisotropic Damage in Fiber-Composites," *Mech. Mater.*, **20**(2), pp. 125–152.
- [25] Hashin, Z., 1980, "Failure Criteria for Unidirectional Fiber Composites," *Trans. ASME, J. Appl. Mech.*, **47**(2), pp. 329–334.
- [26] Roark, R., and Young, W., 1975, *Formulas for Stress and Strain*, 5th ed., McGraw-Hill, Tokyo.